Title

Scaling Laws of Exciton Recombination Kinetics in Low Dimensional Halide Perovskite Nanostructures.

Journal

Journal of the American Chemical Society, 142(19)

ISSN

0002-7863

Authors

Gao, Mengyu
Liu, Hao
Yu, Sunmoon
et al.

Publication Date

2020-05-01

DOI

10.1021/jacs.0c02000

Peer reviewed

Scaling Laws of Exciton Recombination Kinetics in Low Dimensional Halide Perovskite Nanostructures

Mengyu Gao,[†,§] Hao Liu,[‡] Sunmoon Yu,[†,§] Sheena Louisia,[‡,§] Ye Zhang,[‡,§] David P. Nenon,[‡,§] A. Paul Alivisatos,[†,‡,§,∥] and Peidong Yang[†,‡,§,∥,*]

† Department of Materials Science and Engineering, University of California, Berkeley, Berkeley, California 94720, United States

‡ Department of Chemistry, University of California, Berkeley, Berkeley, California 94720, United States

§ Materials Sciences Division, Lawrence Berkeley National Laboratory, Berkeley, California 94720, United States

∥ Kavli Energy NanoScience Institute, Berkeley, California 94720, United States

*Corresponding author. E-mail: p_yang@berkeley.edu (P.Y.)

ABSTRACT

Carrier recombination is a crucial process governing the optical properties of a semiconductor. Although various theoretical approaches have been utilized to describe carrier behaviors, a quantitative understanding of the impact of defects and interfaces in low dimensional semiconductor systems is still elusive. Here we develop a model system consisting of chemically tunable, highly luminescent halide perovskite nanocrystals to illustrate the role of carrier diffusion and material dimensionality on the carrier recombination kinetics and luminescence efficiency. Our advanced synthetic methods provide a well-controlled colloidal system consisting of nanocrystals with different aspect ratios, halide compositions, and surface conditions. Using this system, we reveal the scaling laws of photoluminescence quantum yield and radiative lifetime with respect to the aspect ratio of nanocrystals. The scaling laws derived herein are not only a phenomenological observation but proved a powerful tool disentangling the carrier dynamics of microscopic systems in a quantitative and interpretable manner. The investigation of our model system and theoretical formulation bring to light the dimensionality as a hidden constraint on carrier dynamics and identify the diffusion length as an important parameter that distinguishes nanoscale and macroscale carrier behaviors. The conceptual distinction in carrier dynamics in different dimensionality regimes informs new design rules for optical devices where complex microstructures are involved.

INTRODUCTION

The candidacy of halide perovskites in optoelectronic applications originates from their ability to realize highly-efficient energy conversion. Perovskite-based solar cells,[1,2] light-emitting devices,[3,4] and radiation detectors[5] are all excellent examples. Such wide applications of halide perovskites also stimulate fundamental studies in diverse fields, among which carrier dynamics, because of its relevance to luminescence efficiency, is of great importance.[6]

Early works on halide perovskites demonstrate their intriguing carrier transport properties, including their long charge carrier diffusion length,[7,8] long lifetime,[9] low deep-trap density,[10] etc. Recent findings regarding the microstructures of thin-film devices, however, have shown the complexities related to the inhomogeneity of real systems.[11–13] Due to the involvement of various chemical species and complicated microenvironment, the mechanisms governing the specific light-matter interactions that impair the device performance are under debate.[6,14,15] A better understanding of the impact of defects and dimensionality requires well-defined model systems that permit precise structural determination and systematic study of optical properties.

Precise control on the synthesis of nanocrystals (NCs) is a promising approach to unravel the complexities associated with heterogeneous interfaces. Due to their high uniformity and excellent luminescence efficiency, together with molecular-level probes that afford accurate structural characterizations, NCs have been utilized to understand the electronic structures,[16] thermodynamics,[17,18] and transport properties[19,20] of semiconductors. On the other hand, investigations of colloidal NCs carried within the field of halide perovskites can simultaneously uncover other aspects looking into the “localized” carrier dynamics within single domain of each NC.[21–26] Systems consisting of well-controlled NCs, therefore, open new opportunities in the investigation of optical properties of halide perovskites.

With extensive synthetic efforts and theoretical formulations in the halide perovskite research, different models are employed to describe optical phenomena in (1) low-dimensional, confined systems[22,27] or (2) extended, macroscopic systems.[28,29] However, little attention has been paid to connect the two seemingly irreconcilable length scales. Integrating the local and global pictures of carrier dynamics is thus essential to the better understanding of the electronic processes, which will inform improved design of perovskite-based devices.

In this work, we establish a model system for the systematic investigation of the carrier dynamics in halide perovskites using highly luminescent and well-controlled NCs. Relying on the advanced synthesis of halide perovskite colloidal NCs, we take advantage of the large flexibility of tunable variables including aspect ratio, composition and surface condition to access physical properties of halide perovskite nanostructures. Static photoluminescence quantum yield measurement (PLQY) and time-resolved PL lifetime measurement reveal the intriguing aspect ratio dependent carrier recombination kinetics of NCs, highlighting the distinguishable 0D and 1D carrier dynamics. The direct interpretation of size scaling behaviors in terms of carrier diffusion and recombination is corroborated by time-resolved PL analysis and theoretical modelling.

RESULTS AND DISCUSSION

Building a model system of halide perovskite NCs. To avoid the interference of microstructural heterogeneity, we established a platform for the systematic property studies consisting of high-quality halide perovskite NCs with different aspect ratios and compositions. Modified based on our previous recipe,[30,31] the time-controlled synthesis of colloidal $CsPbBr_3$ NCs yields nanowires with high purity and size homogeneity. We observed that nanowire length grew linearly with reaction time at the fixed reaction temperature, with the growth speed at around 3.7 nm/sec (Fig. 1b). Colloidal $CsPbBr_3$ quantum dots with a similar diameter dispersion were also synthesized[32] to construct a library of NCs with different dimensions. NCs (including nanowires and quantum dots) with aspect ratio ranging from 1 to 10^3 show decent size homogeneity (with diameter of 9.5 ± 1.5 nm, and standard deviation of length of around 20 %), and are morphologically pure (Fig. 1a). The crystallinity and growth directions of $CsPbBr_3$ NCs were confirmed by powder X-ray diffraction (Fig. S5), atomic resolution high-angle annular dark-field imaging (Fig. S2), conventional high resolution transmission electron microscopy (HR TEM) images (Fig. 1c).

Although this synthetic protocol yields single-crystalline, phase-pure nanowires with controllable aspect ratios, the luminescence efficiencies are initially poor (PLQY ~1%), as the centrifugation as a purification method is known to remove the majority of passivating ligands. To investigate the carrier dynamics in systems with excellent optical properties, we turned to surface passivation strategies to improve PLQY. Due to the soft-hard mismatch of oleate and lead cations, the routinely used oleic acid-oleylamine (OA-OAm) pair could only improve the efficiency up to 20% for short nanowires[32,33]. The use of softer anionic ligand (hexylphosphonic acid, HPA) together with OAm for surface treatment on halide perovskite quantum dots proved as the best way to improve the PLQY of perovskite NCs[33]. We therefore adopted the similar ligand exchange method, where the as-

synthesized nanowires were purified thoroughly to remove the native ligand shell, and then HPA-OAm was used as new ligand treatment to restore the surface passivation. The resulting improvement of PLQY by ligand engineering is significant (from ~1% to 20-60%). We also reproduced the surface treatment on quantum dots whose PLQY could be increased up to unity. Though difficulties exist for probing the surface condition of halide perovskite NCs, owing to the dynamic interaction of surface ligands with halide perovskite NCs surface atoms, we were able to probe the strong interaction of the soft acid-base pair with halide perovskite NCs surfaces through 2D nuclear Overhauser effect spectroscopy (2D NOESY) experiments. The negative cross peaks in the 2D NOESY spectrum indicated the tumbling of ligands with slowed relaxation rate due to the interaction between ligands and NC surfaces (Fig. S8),[34] which demonstrates the generality of this ligand exchange method on both 0D quantum dots and 1D nanowires.

Anion exchange of perovskite NCs is well established[31,35–39] and allows us to expand current $CsPbBr_3$ NCs system into other halide compositions, which helps to determine whether our findings are generalizable beyond pure $CsPbBr_3$ compositions. We fully converted $CsPbBr_3$ NCs into $CsPbI_3$, without altering the morphology, size distribution, and crystallinity (Fig. 1d). The same anion exchange reaction was done on the NCs of different aspect ratios (Fig. S1). Exchanging the anionic sublattice from bromide to iodide produces the expected red shift in both absorbance and PL spectra. The PL peak positions shift from 515 nm to 680 nm by fully converting bromide NCs into iodide NCs (Fig. 2a).[31]

The advanced synthetic methods afford an ideal model system consisting of $CsPbBr_3$ and anion-exchanged $CsPbI_3$ NCs with the same diameter and different aspect ratios. After surface treatment, all those NCs were passivated with the same ligand pairs and exhibited high PLQY (100% for 0D NCs, and up to 85% for 1D NCs). The improved quality of NCs due to well-

designed surface chemistry enables the reproducible and quantitative studies, while the purity and controllability of halide perovskite NCs allow us to study their photophysics in a systematic way.

Scaling laws of optical properties of halide perovskite NCs. With a model system in hand, we used steady-state PLQY and time-resolved PL lifetime measurements to investigate carrier dynamics across a wide range of aspect ratios. Together, these two techniques determine the recombination kinetics, thereby informing the key carrier dynamics of the system of interest. PLQY was determined by a home-built integrating sphere system,[40] and PL lifetime was calculated from time-resolved PL measurement (Fig. 2b). These measurements revealed an intriguing dependence on the aspect ratio.

The aspect-ratio-dependent data are shown in Fig. 2c. From the experimental data, there is a clear trend that NCs with larger aspect ratio have lower PLQY, and this trend also applies to different colloidal systems, such as those with different compositions, different surface conditions and different synthetic methods (Fig. S13, Fig. S14). The linear plot of PLQY as a function of aspect ratio shows that PLQY decreases with increased aspect ratio, and reaches a plateau upon a certain critical length. The estimated critical length scale for $CsPbBr_3$ and $CsPbI_3$ NCs is around 500-800 nm. The PLQY plateau for $CsPbBr_3$ NCs is around 20% and that for $CsPbI_3$ NCs is around 50%. For the lowest aspect ratio, which is for quantum dots with cubic shape, PLQY is almost unity for both $CsPbBr_3$ and $CsPbI_3$ NCs. The PL lifetime of those nanocrystals also exhibits a length-dependent trend (Fig. S9). For $CsPbBr_3$ NCs with increased aspect ratio, the averaged PL lifetime increased from 5 ns to tens of nanoseconds, and for $CsPbI_3$ NCs, the averaged PL lifetime increased from 20 ns to hundreds of nanoseconds, both consistent with reported PL lifetime for quantum dots and nanowires.[31,32] We summarized the size-dependent optical properties of halide perovskite NCs

as “scaling laws”. Explicitly, the scaling law describes the relation between a property (f) and the size (V) of a material, $f(V)$. In our scenario, the size V is linearly proportional to the length. The scaling laws defined in this way are not only an important attribute of NCs, but also an essential characteristic component that defines low-dimensional semiconductors.[41,42]

Validity of the scaling laws of halide perovskite NCs. Before the theoretical analysis of the observed scaling laws, the validity and generality of the experimental observations need to be demonstrated. Our later analysis and modelling are based on the assumption that all NCs have similar surface condition and defect density. As mentioned in previous sections, the diameters of all NCs are uniform at around 9.5 nm (Fig. S4), so both the surface area and volume linearly scale with the aspect ratio or length of NCs. X-ray photoemission spectroscopy (XPS) was conducted to probe the surface condition of NCs with different aspect ratios, which revealed the halide-lean surface for halide perovskite NCs, and NCs of different dimensions all shared similar surface stoichiometry (Fig. S7, Tab. S1). By tuning only NC length and composition, with all other synthesis parameters being well-controlled, the measurements from such samples will highlight length- and composition-specific information only. Other evidence of the aspect ratio related scaling law was done by sonicating as-synthesized long nanowires. Sonication broke down the nanowires into shorter ones and this treatment resulted in increased PLQY (Fig. S13). Considering the deleterious effect usually imposed by sonication, the improvement of PLQY indicates the generality of our experimental observation. Similar scaling law of PLQY has also been observed for NCs with different surface environments (Fig. S14). Power dependent PL measurements (Fig. 2c) together with power dependent time-resolved PL measurements demonstrate that the linear kinetics governs the recombination pathway in halide perovskite NCs in our study. This linearity rules out the possible higher order recombination

pathways, such as bimolecular free-carrier recombination, Auger recombination, exciton-exciton interaction, etc. This linear kinetics also suggests that excitons are main carriers in the diffusion and recombination processes. With the assumption of commensurability among all dimensions and the generality of the scaling law, we now turn to theoretical modelling to identify the key factors that underlie our experimental observations.

Modelling of PLQY and carrier dynamics. To understand the size scaling of optical properties, we resorted to the theoretical frameworks of carrier dynamics. The continuity equation with spatial and temporal evolution of carrier density is one of the formal ways to describe carrier behaviors in bulk semiconductors. Although the continuity equation generally remains valid for the confined system, it requires reformulation to account for the large heterogeneity of nonradiative recombination kinetics and explicit spatial boundary conditions (see Supplementary Information (SI)). As will be shown later, the dimensionality will play a signification role modulating the carrier dynamics in confined systems when defect density is relatively low. The incompatibility of models in extended and confined systems poses a difficulty[43–45] in using a single continuity equation to describe our system, where the aspect ratio spans from 0D to 1D. As a result, instead of solving the set of continuity equations, we conducted a Monte Carlo simulation with a exciton-diffusion-defect-encounter random walk model.

As observed in the scaling law of PL lifetime, the NCs with large aspect ratio exhibits prolonged lifetime, while the power dependent time-resolved PL measurements preclude the existence of free-carrier-dominant recombination channels. So in addition to the typical radiative and nonradiative recombination processes, we introduced a detrapping process, through which the trapped excitons can be released with some probability. Trapping-detrapping mechanisms are classically adopted in the semiconductor community[46,47] and have been recently brought up as an

alternative explanation to the PL blinking phenomena and prolonged radiative lifetimes.[48] In the context of halide perovskite, trapping/detrapping process is highly relevant to its defect tolerance.

In each random walk, we tracked the trajectory of each exciton and collected all the dynamic information. From this, PLQY and carrier recombination decays as ensemble observables can be easily retrieved. We performed both a “local” fitting and a “global” fitting, where the former technique was intended to extract carrier dynamical parameters (defect density, exciton diffusivity, exciton radiative recombination rate, etc.) from the time-resolved PL curves, while the later one was aimed at reproducing the scaling laws by assuming the constant aforementioned carries dynamical parameters.

From the local fitting of time-resolved PL experiments (Fig. S11, Fig. S12), we extract the main carrier dynamical parameters from six representative batches of $CsPbBr_3$ NCs (Tab. 1). We found that although the apparent averaged lifetime is increased from shorter (~8) to longer aspect ratios (~180), the radiative recombination rate is almost constant in the NWs regimes. Considering that the Bohr radius of $CsPbBr_3$ is around 7 nm, the reduced dielectric screening and quantum confinement due to elongation of NWs plays little role altering the exciton radiative recombination kinetics. The local fitting results also proved the homogeneity of our model system, that is, the consistency of carrier dynamical parameters. With the assumption that NCs with different aspect ratios share similar carrier dynamical parameters, we performed the global fitting by varying the aspect ratio, therefore, reproducing the scaling laws observed experimentally. The global fitting is shown in Fig. 3a, whereby we determined the *linear* defect density as 0.005 effective defects per nanometer (abbreviated as 1/nm thereafter) and 0.0016 1/nm for $CsPbBr_3$ and $CsPbI_3$ respectively. We transformed the linear defect density into bulk defect density taking into account the diameter of NCs. The bulk defect density is determined as 5.0×10^{16} $1/cm^3$ for $CsPbBr_3$ and 1.6×10^{16} $1/cm^3$ for $CsPbI_3$, which respectively

share a similar order of magnitude with our previous results.[31] One usually overlooked fact about the defect density, as reported in the literature, lies where the defect density only counts the time average of fully-functioning trap states. Dominant defect species in halide perovskite (especially in $CsPbBr_3$ and $CsPbI_3$), such as halide or cesium vacancies, only introduce shallow trapping levels or barely contribute to luminescence efficiency.[10,32,33] So in general electrical or optically defined and determined defect density will be significantly lower than the density of physically present vacancies,[33] and the apparent discrepancy between the two types of values is a signature of the well-known defect tolerance of halide perovskites. The exciton diffusivity were determined as 0.4 cm^2/s, which is comparable with the literature.[7,8,10,49,50] As mentioned above, in order to explain prolonged PL lifetime, we need to include detrapping process. With delayed time of around 100 ns, we were able to fit the lifetime results with our simulation (Fig. 3b). Without a detrapping process, however, simulated results showed a decreased lifetime with increasing aspect ratio (Fig. 3b), which is contradictory to the experimental observations. The physical meaning of this number is still under investigation but comparable with other NCs systems.[48,51]

Size scaling in the NCs literature. The aspect ratio dependent optical properties of 1D semiconductor NCs have been reported in diverse systems, notably in traditional covalent II-VI or III-V semiconductor nanorods/nanowires and carbon nanotubes. Because of the synthetic limitations and phase complexity, the aspect ratio of single crystalline nanorods is usually limited below 100 or even 20.[52–58] There are some recent results also concerning the low-aspect-ratio perovskite nanorods, but those NCs also suffer from both limited length scale and unknown surface condition.[58,59] In such small aspect ratio regime, wave function extension will be modified with changing aspect ratio, thus giving rise to the renormalized

electronic energy levels,[60,61] and imposing more complexities on the analysis of PLQY[60,62,63] and recombination dynamics.[58,60,64–66] In our system, due to advanced synthetic control, the aspect ratio of halide perovskite NCs ranges from 1 to 1000, far exceeding the quantum mechanical regime. We therefore exclude complexities due to the band gap renormalization, and the carrier dynamics can be treated semi-classically.

The PLQY scaling in large aspect ratio system is well documented in the optical studies of carbon nanotubes.[67–70] However, the size scaling trend of carbon nanotubes is the opposite to our case, where a smaller aspect ratio results in a lower PLQY. This is due to the quenching sites found on the ends of the carbon nanotube.[69,71] In other words, the defect density decreases as the nanotube grows longer. In our system, however, due to the well-controlled surface chemistry, we could modify the surface and maintain a constant defect density among different aspect ratios. This was corroborated by the carrier dynamics analysis (Tab.1) and XPS measurement (Tab. S1).

Due to a better synthetic control over dimensionality, composition and surface condition of halide perovskite NCs, high crystal quality and size uniformity help to exclude potential complications from microstructures. The realization of the continuity from quasi-0D to 1D NCs, simply put, that of the chemical tunability, reveals the hidden constraint of dimensionality on carrier dynamics. We are therefore able to tackle the scaling laws from a new perspective, while constructing a revised and unified view on carrier dynamics in low-dimensional semiconductors.

The scaling laws of optical properties in halide perovskite and theoretical analysis suggest that the description of carrier dynamics in nanoscale compared with that in bulk semiconductors requires careful reformulation, notably when the non-radiative recombination rate k_{nr} turns out to be size-dependent as the carriers are confined by microscopic boundaries (see SI). That is why we resorted to a Monte Carlo random walk model to simulate the global fitting of the scaling laws. With this model, we bridged the gap

between quasi-0D and 1D carrier behaviors directly while circumventing the complexity of continuity equation and the difficulty in solving the first passage process analytically.[43–45] In the preceding sections, we not only reproduced the experimental results, but identified a critical length scale that distinguishes the carrier dynamical behaviors in 0D and 1D. Given the advantages of our NCs system and the flexibility of our simulation method, in the following section, we will examine the physical origin of the scaling laws and demonstrate the generics of this size-scaling methodology.

Interpreting the scaling laws. To interpret the scaling laws in an intuitive way, we first need to investigate the very length scale on which physical processes are happening. In our system, three types of length scale are of interest, (1) the length of the nanowire l, (2) the average distance between defects l_d (inverse of the *linear* defect density ρ), and (3) the diffusion length l_r (which is here defined as $l_r^2 = D\tau_r$). Assuming ρ is small, we derived an asymptotic expression based on two extreme limits of l (see SI): When l approaches infinity, PLQY = $1-\alpha l_r/l_d$ (where α is a proportional constant); when l is infinitesimally small, PLQY = $1-l/l_d$.

When l goes to the bulk limit, in both experimental and simulation results, we observed the length-independent plateau where NCs with large aspect ratio behave more like bulk materials than nanomaterials, which is corresponding to a length-independent and diffusion-limited PLQY. The diffusivity plays an important role because the mobility of excitons determines how efficient the radiative recombination compete with the interruption of diffusion and radiative recombination by defects. We call this regime the *diffusion-limited regime*.

In the length scale where l is on a similar order of l_r, we observed a drastically different behavior, that is, the PLQY starts to be less dependent on the carrier diffusivity (Fig. 4b, Fig. S18). When l approaches zero, the influence of diffusion disappears. Due to the confined nature in this length

scale, we call this regime the *spatially-confined regime*. In this regime, the free diffusion of carriers is impaired by the impermeable boundaries imposed by the length of certain NC, thus preventing excitons being influenced by defects in other NCs. The interplay between defect density and the length of NCs is manifested in the expression, PLQY = $1-l/l_d$, and Fic. 4a and Fig. 4c show that the initial slope of PLQY-length curve is proportional to the defect density ($\rho=1/l_d$), while almost independent of the carrier diffusivity.

The demarcation between diffusion-limited regime and spatially-confined regime is graphically determined as the intersection between the initial slope and final plateau and is denoted as $l_{critical}$. Based on the asymptotic analysis, this critical length is proportional to diffusion length, $l_{critical} = \alpha l_r$. Fig. 4d demonstrates the near linearity of diffusion length and critical length, and this linearity can be derived through the classical semiconductor statistics as well (see SI).

The direct interpretability of the observed scaling laws lies in the simplicity of the asymptotic expression in either regime and the small number of parameters involved. The important carrier dynamical parameters can be extracted from those geometrical characteristics of the scaling laws in a straightforward manner. Due to the generality of our theoretical derivation, we propose that this methodology could be applied to other materials systems and other dimensionalities.

CONCLUSIONS AND NEW PERSPECTIVES

The capacity of realizing the morphologically- and compositionally-controlled system in a flexible and systematic way enables us to investigate the defect-efficiency relation of halide perovskite from a new perspective. We take this advantage to demonstrate the size scaling as a powerful tool to elucidate the carrier dynamics in low-dimensional semiconductors. Distinguished from other techniques, the scaling laws derived here afford both simplicity and interpretability to the analysis of carrier dynamics. Experimentally, our study bridges two dimensions (0D and 1D or, in a general sense, nanoscale and macroscale), and identifies a critical length scale that distinguishes the signatures of carrier dynamics exhibited in different dimensionality regimes. As revealed in our theoretical and numerical analysis, the distinct exciton behaviors and formulations in different dimensionality regimes are the manifestation of how defects locally or globally influence the carrier dynamics and luminescence efficiency. We explicitly denote this distinction of length scales by using the diffusion length, which is highlighted due to its relevance to unifying nanoscale phenomena with the macroscopic systems.

The microstructure of semiconductor devices is one of the key factors that influence the device efficiency. Our system is a novel prototype to mimic the micro-to-macro transition, while eliminating interfacial interferences. The new understanding of carrier dynamics provides a promising approach for the design of high-efficiency semiconductor devices. Informed by the fact that both material dimensionality and carrier diffusion are key factors contributing to the carrier dynamics, engineering the diffusion pathways such as implementing impermeable boundaries or immobile excitons might serve as another mechanism for increased utilization of charge carriers or excitons.

ACKNOWLEDGEMENTS

The authors thank Prof. E. Rabani, Dr. D. Zhang, Dr. Q. Kong, Dr. A. D. Balan, and D. An for fruitful discussions on theoretical formulation, experimental design and computational strategies. This work was primarily supported by the U.S. Department of Energy, Office of Science, Office of Basic Energy Sciences, Materials Sciences and Engineering Division, under Contract No. DE-AC02-05-CH11231 within Physical Chemistry of Inorganic Nanostructures Program (KC3103). Work at the Molecular Foundry was supported by the Office of Science, Office of Basic Energy Sciences, of the U.S. Department of Energy under Contract No. DE-AC02-05CH11231. M.G. acknowledges the Ning Fellowship granted by University of California, Berkeley. Y.Z. acknowledges the fellowship from Suzhou Industrial Park. S.Y. acknowledges support from Samsung Scholarship.

NOTES

The authors declare no competing financial interest.

FIGURES

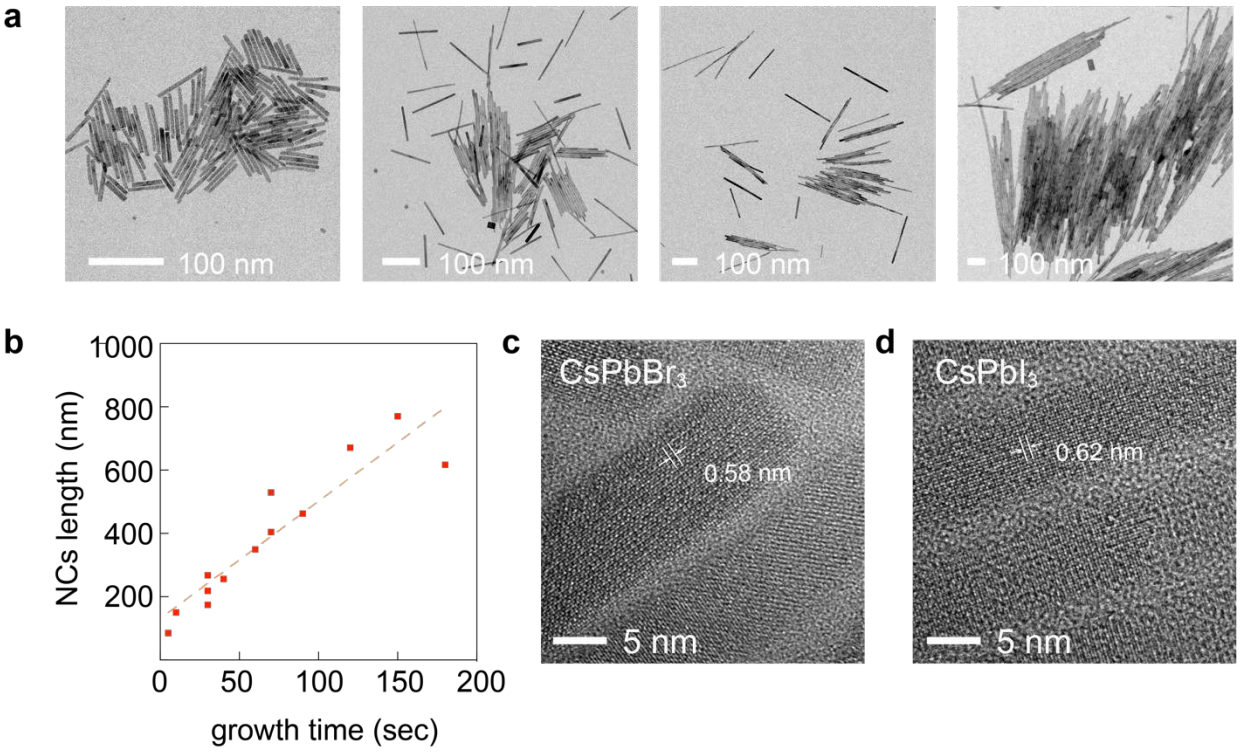

Fig. 1 | TEM characterizations on growth kinetics and crystallography. a, Representative TEM images of $CsPbBr_3$ nanocrystals with different aspect ratios. **b**, Length of NCs as a function of reaction time. **c**,**d**, HR TEM images of $CsPbBr_3$ and $CsPbI_3$ nanowires.

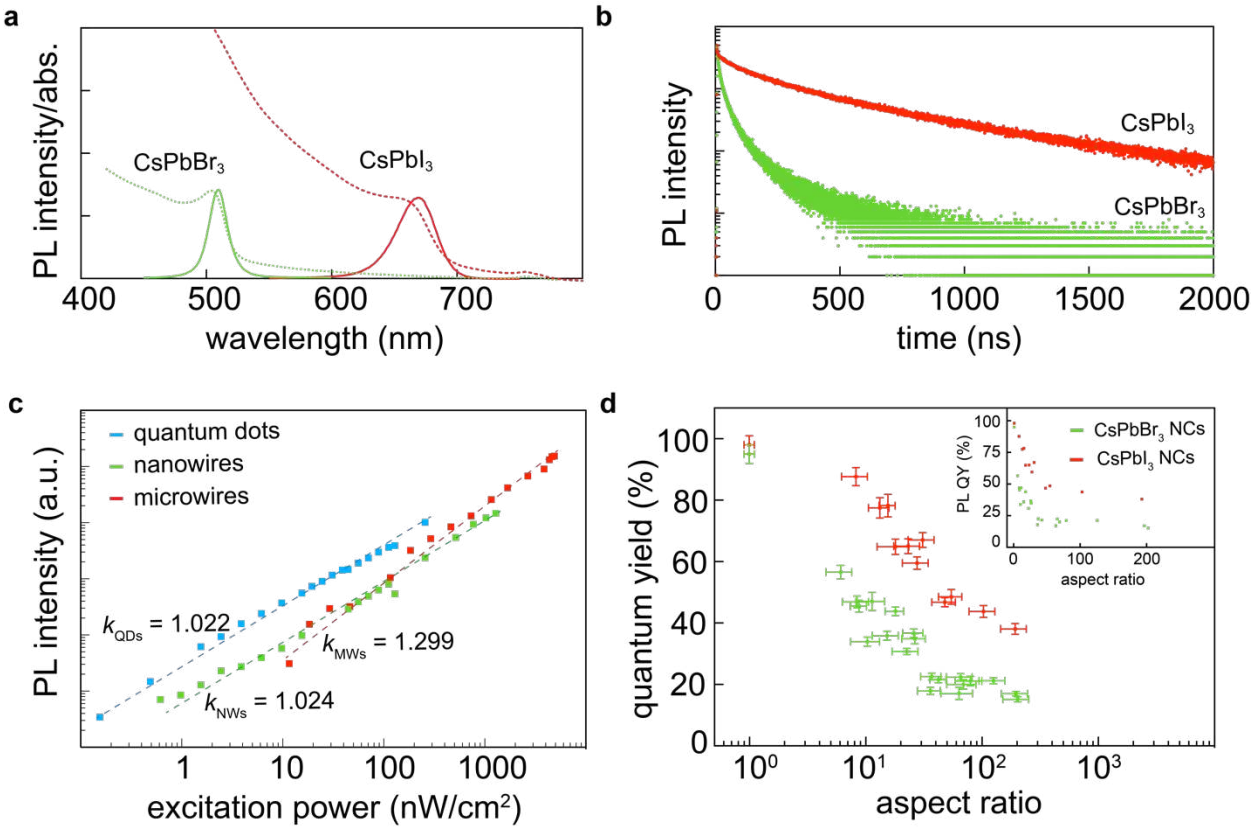

Fig. 2 | Representative optical characterizations and scaling laws of PLQY of $CsPbX_3$ NCs. a, PL and absorption spectra of $CsPbBr_3$ nanowires (green curves) and $CsPbI_3$ nanowires (red curves). **b**, Time-resolved PL decay curves of $CsPbBr_3$ nanowires (green curve) and $CsPbI_3$ nanowires (red curve). **c**, Power-dependent PL measurement for $CsPbBr_3$ quantum dots, nanowires (diameter ~10 nm, length ~ 1000 nm), and microwires (diameter > 100 nm). Slopes of the log plots are indicated by *k*-values for NCs with different dimensions. **d**, Aspect ratio dependent PLQY (scaling law of PLQY) of $CsPbBr_3$ nanocrystals (green data points) and $CsPbI_3$ nanocrystals (red data points). The error bar for *x*-axis showing the deviation of length and that for *y*-axis showing the measurement deviation of quantum yield (inset shows the linear plotting with the same data points, omitting the standard deviations).

Tab. 1 | Main carrier dynamical parameters of $CsPbBr_3$ NCs with different aspect ratios.

Length (nm)	Averaged lifetime (ns)	Radiative lifetime (ns)	Carrier diffusivity (cm^2/s)	defect density ($1/cm^3$)	Detrapping probability	Detrapping time (ns)
9.5 (QDs)	5.3	5.3	0.4	5.00×10^{16}	0.95	120
80 (NWs)	11.4	12	0.4	5.00×10^{16}	0.90	80
122 (NWs)	14.6	13	0.4	4.00×10^{16}	0.88	120
229 (NWs)	18.5	15	0.4	5.00×10^{16}	0.92	120
537 (NWs)	16.3	13	0.4	4.00×10^{16}	0.92	150
1800 (NWs)	17.6	15	0.4	4.00×10^{16}	0.90	160

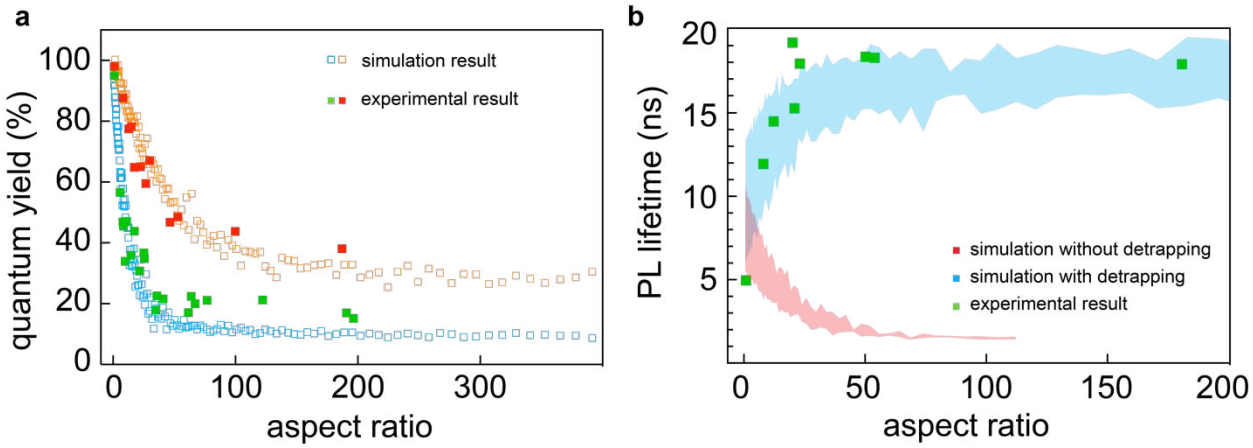

Fig. 3 | Comparison of simulation results with experimental results. **a**, Green solid data points are PLQY measured from $CsPbBr_3$ NCs, while red solid data points are that from $CsPbI_3$ NCs. Blue/Orange hollow data points are simulated for $CsPbBr_3$/$CsPbI_3$ NCs. **b**, Experimental and simulation results for averaged lifetime of $CsPbBr_3$ NCs. Width of the shaded area is from the simulation of lifetime with different parameters (radiative time and defect density).

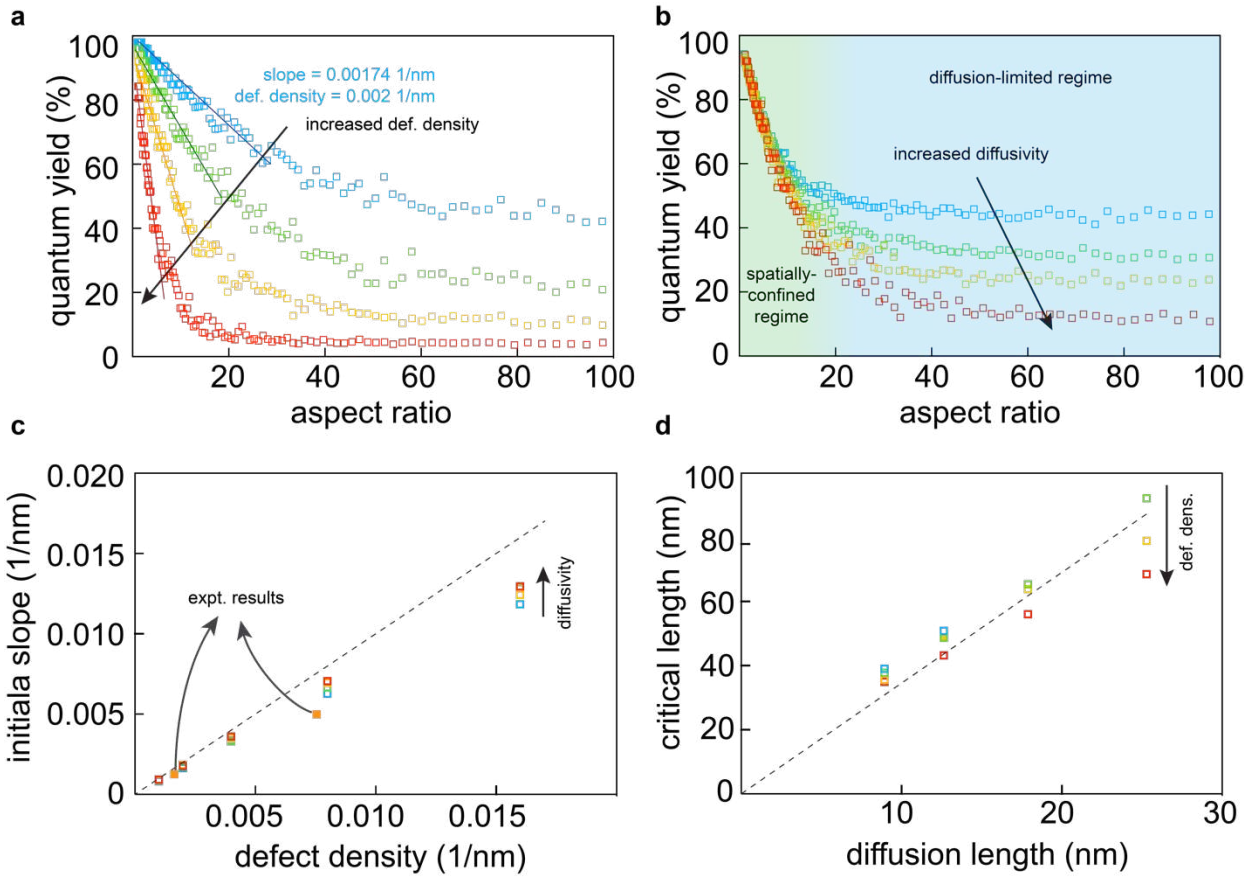

Fig. 4 | Simulated results where defect density and diffusivity are controlled. a, Aspect-ratio-dependent PLQY with various defect density. **b**, Aspect-ratio-dependent PLQY with various carrier diffusivity. Green-shaded area is the division of spatially-confined regime and blue-shaded area is that of diffusion-limited regime. **c**, Demonstration of the linear relation between the initial slope of the QY-length plot and defect density (dashed line is a linear plot with slope of unity). Data points with different colors are from different diffusivities. This figure demonstrates that the initial slope is less dependent on diffusivity when defect density is lower. Two experimental results are from $CsPbBr_3$ and $CsPbI_3$ samples, indicating the defect density of our system is within the linear region where the slope of the scaling law of PLQY reflects the defect density. **d**, Demonstration of the linear relation between critical length (the length upon which PLQY reaches a plateau) and

diffusion length. When diffusivity and defect density are smaller, this linear relation is more prominent.

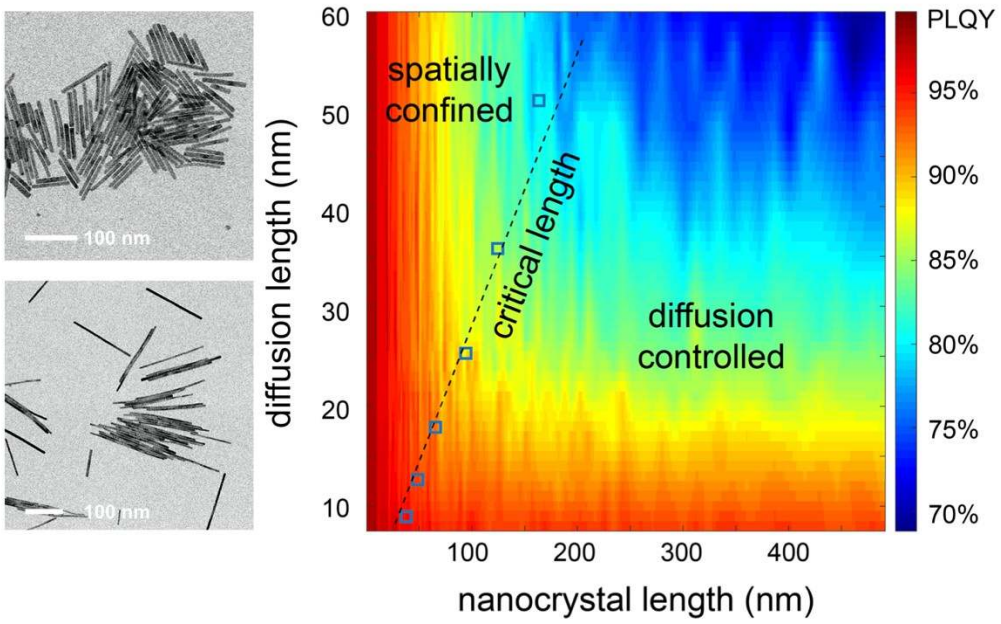

Fig. for Table of Content

REFERENCES

1. Green, M. A., Ho-Baillie, A. & Snaith, H. J. The emergence of perovskite solar cells. *Nat. Photonics* **8**, 506–514 (2014).
2. Tsai, H. *et al.* High-efficiency two-dimensional Ruddlesden–Popper perovskite solar cells. *Nature* **536**, 312–316 (2016).
3. Lin, K. *et al.* Perovskite light-emitting diodes with external quantum efficiency exceeding 20 per cent. *Nature* **562**, 245–248 (2018).
4. Cao, Y. *et al.* Perovskite light-emitting diodes based on spontaneously formed submicrometre-scale structures. *Nature* **562**, 249–253 (2018).
5. Chen, Q. *et al.* All-inorganic perovskite nanocrystal scintillators. *Nature* **561**, 88–93 (2018).
6. Brenner, T. M., Egger, D. A., Kronik, L., Hodes, G. & Cahen, D. Hybrid organic—inorganic perovskites: low-cost semiconductors with intriguing charge-transport properties. *Nat. Rev. Mater.* **1**, 1417–1443 (2016).
7. Stranks, S. D. *et al.* Electron-Hole Diffusion Lengths Exceeding 1 Micrometer in an Organometal Trihalide Perovskite Absorber. *Science* **342**, 341–344 (2013).
8. Xing, G. *et al.* Long-Range Balanced Electron- and Hole-Transport Lengths in Organic-Inorganic CH3NH3PbI3. *Science* **342**, 344–347 (2013).
9. Zhang, M. *et al.* Composition-dependent photoluminescence intensity and prolonged recombination lifetime of perovskite CH3NH3PbBr3-xClx films. *Chem. Commun.* **50**, 11727–11730 (2014).
10. Shi, D. *et al.* Low trap-state density and long carrier diffusion in organolead trihalide perovskite single crystals. *Science* **347**, 519–522 (2015).
11. de Quilettes, D. W. *et al.* Impact of microstructure on local carrier lifetime in perovskite solar cells. *Science* **348**, 683–686 (2015).
12. Grancini, G. *et al.* Role of microstructure in the electron-hole interaction

of hybrid lead halide perovskites. *Nat. Photonics* **9**, 695–701 (2015).

13. Blancon, J. C. *et al.* Extremely efficient internal exciton dissociation through edge states in layered 2D perovskites. *Science* **355**, 1288–1292 (2017).
14. Huang, J., Yuan, Y., Shao, Y. & Yan, Y. Understanding the physical properties of hybrid perovskites for photovoltaic applications. *Nat. Rev. Mater.* **2**, 17019–17042 (2017).
15. Shi, E. *et al.* Extrinsic and Dynamic Edge States of Two-Dimensional Lead Halide Perovskites. *ACS Nano* (2019). doi:10.1021/acsnano.8b07631
16. Norris, D. J., Sacra, A., Murray, C. B. & Bawendi, M. G. Measurement of the size dependent hole spectrum in CdSe quantum dots. *Phys. Rev. Lett.* **72**, 2612–2615 (1994).
17. Goldstein, A. N., Echer, C. M. & Alivisatos, A. P. Melting in Semiconductor Nanocrystals. *Science* **256**, 1425–1427 (1992).
18. Tolbert, S. H. & Alivisatos, A. P. Size Dependence of a First Order Solid-Solid Phase Transition: The Wurtzite to Rock Salt Transformation in CdSe Nanocrystals. *Science* **265**, 373–376 (1994).
19. Chen, R. *et al.* Thermal Conductance of Thin Silicon Nanowires. *Phys. Rev. Lett.* **101**, 1–4 (2008).
20. Hochbaum, A. I. *et al.* Enhanced thermoelectric performance of rough silicon nanowires. *Nature* **451**, 163–167 (2008).
21. Makarov, N. S. *et al.* Spectral and Dynamical Properties of Single Excitons, Biexcitons, and Trions in Cesium–Lead-Halide Perovskite Quantum Dots. *Nano Lett.* **16**, 2349–2362 (2016).
22. Rainò, G. *et al.* Single Cesium Lead Halide Perovskite Nanocrystals at Low Temperature: Fast Single-Photon Emission, Reduced Blinking, and Exciton Fine Structure. *ACS Nano* **10**, 2485–2490 (2016).
23. Isarov, M. *et al.* Rashba Effect in a Single Colloidal CsPbBr 3Perovskite

Nanocrystal Detected by Magneto-Optical Measurements. *Nano Lett.* **17**, 5020–5026 (2017).

24. Becker, M. A. *et al.* Bright triplet excitons in caesium lead halide perovskites. *Nature* **553**, 189–193 (2018).
25. Rainò, G. *et al.* Superfluorescence from lead halide perovskite quantum dot superlattices. *Nature* **563**, 671–675 (2018).
26. Utzat, H. *et al.* Coherent single-photon emission from colloidal lead halide perovskite quantum dots. *Science* eaau7392-9 (2019).
27. Fang, H.-H. *et al.* Exciton Recombination in Formamidinium Lead Triiodide: Nanocrystals versus Thin Films. *Small* **13**, 1700610–1700673 (2017).
28. Stranks, S. D. *et al.* Recombination Kinetics in Organic-Inorganic Perovskites: Excitons, Free Charge, and Subgap States. *Phys. Rev. Appl.* **2**, 433–438 (2014).
29. Herz, L. M. Charge-Carrier Dynamics in Organic-Inorganic Metal Halide Perovskites. *Annu. Rev. Phys. Chem.* **67**, 65–89 (2016).
30. Zhang, D., Eaton, S. W., Yu, Y., Dou, L. & Yang, P. Solution-Phase Synthesis of Cesium Lead Halide Perovskite Nanowires. *J. Am. Chem. Soc.* **137**, 9230–9233 (2015).
31. Zhang, D. *et al.* Synthesis of Composition Tunable and Highly Luminescent Cesium Lead Halide Nanowires through Anion-Exchange Reactions. *J. Am. Chem. Soc.* **138**, 7236–7239 (2016).
32. Koscher, B. A., Swabeck, J. K., Bronstein, N. D. & Alivisatos, A. P. Essentially Trap-Free CsPbBr 3Colloidal Nanocrystals by Postsynthetic Thiocyanate Surface Treatment. *J. Am. Chem. Soc.* **139**, 6566–6569 (2017).
33. Nenon, D. P. *et al.* Design Principles for Trap-Free CsPbX3 Nanocrystals: Enumerating and Eliminating Surface Halide Vacancies with Softer Lewis Bases. *J. Am. Chem. Soc.* **140**, 17760–17772 (2018).

34. Hens, Z. & Martins, J. C. A Solution NMR Toolbox for Characterizing the Surface Chemistry of Colloidal Nanocrystals. *Chem. Mater.* **25**, 1211–1221 (2013).

35. Dou, L. *et al.* Spatially resolved multicolor CsPbX 3nanowire heterojunctions via anion exchange. *Proc. Natl. Acad. Sci.* **114**, 7216–7221 (2017).

36. Nedelcu, G. *et al.* Fast Anion-Exchange in Highly Luminescent Nanocrystals of Cesium Lead Halide Perovskites (CsPbX 3, X = Cl, Br, I). *Nano Lett.* **15**, 5635–5640 (2015).

37. Koscher, B. A., Bronstein, N. D., Olshansky, J. H., Bekenstein, Y. & Alivisatos, A. P. Surface- vs Diffusion-Limited Mechanisms of Anion Exchange in CsPbBr 3Nanocrystal Cubes Revealed through Kinetic Studies. *J. Am. Chem. Soc.* **138**, 12065–12068 (2016).

38. Ning, C.-Z., Dou, L. & Yang, P. Bandgap engineering in semiconductor alloy nanomaterials with widely tunable compositions. *Nat. Rev. Mater.* **2**, 1–15 (2017).

39. Zhang, Y. *et al.* Quantitative imaging of anion exchange kinetics in halide perovskites. *Proc. Natl. Acad. Sci.* **116**, 12648 LP-12653 (2019).

40. Bronstein, N. D. *et al.* Quantum Dot Luminescent Concentrator Cavity Exhibiting 30-fold Concentration. *ACS Photonics* **2**, 1576–1583 (2015).

41. Alivisatos, A. P. Perspectives on the Physical Chemistry of Semiconductor Nanocrystals. *J. Phys. Chem.* **100**, 13226–13239 (1996).

42. Manna, L., Scher, E. C. & Alivisatos, A. P. Shape Control of Colloidal Semiconductor Nanocrystals. *J. Clust. Sci.* **13**, 521–532 (2002).

43. Montroll, E. W. Random Walks on Lattices. III. Calculation of First-Passage Times with Application to Exciton Trapping on Photosynthetic Units. *J. Math. Phys.* **10**, 753–765 (1969).

44. Opplestrup, T., Bulatov, V. V., Gilmer, G. H., Kalos, M. H. & Sadigh, B. First-passage Monte Carlo algorithm: Diffusion without all the hops.

Phys. Rev. Lett. **97**, 10–13 (2006).

45. Blumen, A., Klafter, J. & Zumofen, G. Recombination in amorphous materials as a continuous-time random-walk problem. *Phys. Rev. B* **27**, 3429–3435 (1983).
46. Maiberg, M., Hölscher, T., Zahedi-Azad, S. & Scheer, R. Theoretical study of time-resolved luminescence in semiconductors. III. Trap states in the band gap. *J. Appl. Phys.* **118**, 105701–105711 (2015).
47. Blakemore, J. S. *Semiconductor statistics.* (New York : Dover, c1987., 1987).
48. Rabouw, F. T. *et al.* Delayed Exciton Emission and Its Relation to Blinking in CdSe Quantum Dots. *Nano Lett.* **15**, 7718–7725 (2015).
49. Saidaminov, M. I. *et al.* High-quality bulk hybrid perovskite single crystals within minutes by inverse temperature crystallization. *Nat. Commun.* **6**, 1–6 (2015).
50. Tian, W., Zhao, C., Leng, J., Cui, R. & Jin, S. Visualizing Carrier Diffusion in Individual Single-Crystal Organolead Halide Perovskite Nanowires and Nanoplates. *J. Am. Chem. Soc.* **137**, 12458–12461 (2015).
51. Chirvony, V. S. *et al.* Delayed Luminescence in Lead Halide Perovskite Nanocrystals. *J. Phys. Chem. C* **121**, 13381–13390 (2017).
52. Alivisatos, A. P. *et al.* Shape control of CdSe nanocrystals . *Nature* **404**, 59–61 (2000).
53. Sapra, S., Poppe, J. & Eychmüller, A. CdSe Nanorod Synthesis: A New Approach. *Small* **3**, 1886–1888 (2007).
54. Carbone, L. *et al.* Synthesis and Micrometer-Scale Assembly of Colloidal CdSe/CdS Nanorods Prepared by a Seeded Growth Approach. *Nano Lett.* **7**, 2942–2950 (2007).
55. Wang, W., Banerjee, S., Jia, S., Steigerwald, M. L. & Herman, I. P. Ligand Control of Growth, Morphology, and Capping Structure of Colloidal CdSe Nanorods. *Chem. Mater.* **19**, 2573–2580 (2007).

56. Placencia, D., Boercker, J. E., Foos, E. E. & Tischler, J. G. Synthesis and Optical Properties of PbSe Nanorods with Controlled Diameter and Length. *J. Phys. Chem. Lett.* **6**, 3360–3364 (2015).

57. Bae, W. K. *et al.* Controlling the influence of Auger recombination on the performance of quantum-dot light-emitting diodes. *Nat. Commun.* **4**, 1–8 (2013).

58. Yang, D. *et al.* Interfacial Synthesis of Monodisperse CsPbBr3 Nanorods with Tunable Aspect Ratio and Clean Surface for Efficient Light-Emitting Diode Applications. *Chem. Mater.* 1–9 (2019).

59. Tong, Y. *et al.* Chemical Cutting of Perovskite Nanowires into Single-Photon Emissive Low-Aspect-Ratio CsPbX 3 (X=Cl, Br, I) Nanorods. *Angew. Chemie - Int. Ed.* **57**, 16094–16098 (2018).

60. She, C., Demortière, A., Shevchenko, E. V & Pelton, M. Using Shape to Control Photoluminescence from CdSe/CdS Core/Shell Nanorods. *J. Phys. Chem. Lett.* **2**, 1469–1475 (2011).

61. Steiner, D. *et al.* Zero-dimensional and quasi one-dimensional effects in semiconductor nanorods. *Nano Lett.* **4**, 1073–1077 (2004).

62. Mokari, T. & Banin, U. Synthesis and Properties of CdSe / ZnS Core / Shell Nanorods Synthesis and Properties of CdSe / ZnS Core / Shell Nanorods. *Chem. Mater.* **15**, 3955–3960 (2003).

63. Geißler, D., Würth, C., Wolter, C., Weller, H. & Resch-Genger, U. Excitation wavelength dependence of the photoluminescence quantum yield and decay behavior of CdSe/CdS quantum dot/quantum rods with different aspect ratios. *Phys. Chem. Chem. Phys.* **19**, 12509–12516 (2017).

64. Bellessa, J. *et al.* Quantum-size effects on radiative lifetimes and relaxation of excitons in semiconductor nanostructures. *Phys. Rev. B* **58**, 9933–9940 (1998).

65. Htoon, H., Hollingsworth, J. A., Dickerson, R. & Klimov, V. I. Effect of

Zero- to One-Dimensional Transformation on Multiparticle Auger Recombination in Semiconductor Quantum Rods. *Phys. Rev. Lett.* **91**, 227401 (2003).

66. Padilha, L. A. *et al.* Aspect Ratio Dependence of Auger Recombination and Carrier Multiplication in PbSe Nanorods. *Nano Lett.* **13**, 1092–1099 (2013).
67. Rajan, A., Strano, M. S., Heller, D. A., Hertel, T. & Schulten, K. Length-Dependent Optical Effects in Single Walled Carbon Nanotubes †. *J. Phys. Chem. B* **112**, 6211–6213 (2008).
68. Hertel, T., Himmelein, S., Ackermann, T., Stich, D. & Crochet, J. Diffusion Limited Photoluminescence Quantum Yields in 1-D Semiconductors: Single-Wall Carbon Nanotubes. *ACS Nano* **4**, 7161–7168 (2010).
69. Moritsubo, S. *et al.* Exciton Diffusion in Air-Suspended Single-Walled Carbon Nanotubes. *Phys. Rev. Lett.* **104**, 247402–247404 (2010).
70. Harrah, D. M. & Swan, A. K. The Role of Length and Defects on Optical Quantum Efficiency and Exciton Decay Dynamics in Single-Walled Carbon Nanotubes. *ACS Nano* **5**, 647–655 (2010).
71. Ishii, A., Yoshida, M. & Kato, Y. K. Exciton diffusion, end quenching, and exciton-exciton annihilation in individual air-suspended carbon nanotubes. *Phys. Rev. B* **91**, 125410–125427 (2015).
72. Lu, D. *et al.* Giant Light-Emission Enhancement in Lead Halide Perovskites by Surface Oxygen Passivation. *Nano Lett.* **18**, 6967–6973 (2018).